

Photocatalytic H<sub>2</sub> Evolution

How to cite:

International Edition: doi.org/10.1002/anie.202301239

German Edition: doi.org/10.1002/ange.202301239

# Cd/Pt Precursor Solution for Solar H<sub>2</sub> Production and in situ Photochemical Synthesis of Pt Single-atom Decorated CdS Nanoparticles

Pankaj Sharma,\* Monika Sharma, Malcolm Dearg, Martin Wilding, Thomas J. A. Slater, and C. Richard A. Catlow\*

**Abstract:** Despite extensive efforts to develop high-performance H<sub>2</sub> evolution catalysts, this remains a major challenge. Here, we demonstrate the use of Cd/Pt precursor solutions for significant photocatalytic H<sub>2</sub> production (154.7 mmol g<sup>-1</sup> h<sup>-1</sup>), removing the need for a pre-synthesized photocatalyst. In addition, we also report simultaneous in situ synthesis of Pt single-atoms anchored CdS nanoparticles (Pt<sub>SA</sub>-CdS<sub>IS</sub>) during photoirradiation. The highly dispersed in situ incorporation of extensive Pt single atoms on CdS<sub>IS</sub> enables the enhancement of active sites and suppresses charge recombination, which results in exceptionally high solar-to-hydrogen conversion efficiency of ≈1% and an apparent quantum yield of over 91% (365 nm) for H<sub>2</sub> production. Our work not only provides a promising strategy for maximising H<sub>2</sub> production efficiency but also provides a green process for H<sub>2</sub> production and the synthesis of highly photoactive Pt<sub>SA</sub>-CdS<sub>IS</sub> nanoparticles.

which determines the efficiency, scalability, and cost-competitiveness of the system. However, the design of an efficient photocatalyst can be challenging,<sup>[7,9–16]</sup> both regarding the synthesis methods and the role of co-catalysts. In most previous studies,<sup>[7,10,17–24]</sup> photocatalyst synthesis protocols involved solvothermal, hydrothermal, and organic solution methods followed by multiple steps including co-catalyst loading, surface shielding, conjugation, and hybridisation. In contrast to this requirement for a pre-synthesized photocatalyst, the direct use of a photoactive reaction solution for solar H<sub>2</sub> production mitigates the use of multi-step synthesis methods, high-cost organic solvents, sophisticated reaction setup, additional thermal treatments and co-catalyst loading. From the perspective of practical feasibility and environmental impact, the elimination of separate synthesis steps for any photocatalyst would be very desirable.

In this paper, we report effective solar H<sub>2</sub> production (154.7 mmol g<sup>-1</sup> h<sup>-1</sup> from Cd-Pt<sub>2</sub>-SSs suspension) by direct solar irradiation of an aqueous suspension of Cd (cadmium nitrate) and Pt (chloroplatinic acid) metal precursors in sodium sulphide (Na<sub>2</sub>S, 0.25 M) + sodium sulphite (Na<sub>2</sub>SO<sub>3</sub>, 0.35 M) solution (SSs), termed as Cd<sub>x</sub>-Pt<sub>y</sub>-SSs. Importantly, the direct use of a precursor suspension, without using any complex photocatalyst synthesis process and organic solvents, outperforms most of the earlier reported photocatalysts for H<sub>2</sub> production for particulate systems that we will show later in this paper. Furthermore, the simultaneous in situ formation of Pt single-atoms anchored CdS nanoparticles (Pt<sub>SA</sub>-CdS<sub>IS</sub>) shows the efficacy of the strategy (Scheme 1). Thus, we demonstrate a promising, environmentally benign, and cost-effective strategy for efficient H<sub>2</sub> production, as well as for the synthesis of metal-semi-

## Introduction

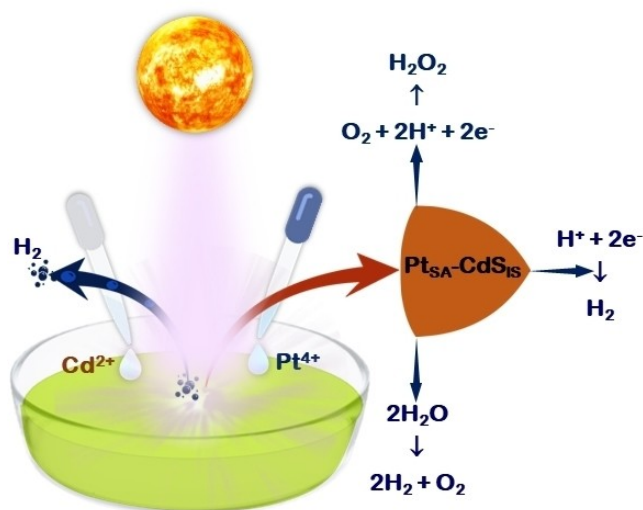
Solar energy may be stored chemically as well as electrically.<sup>[1–4]</sup> Harvesting solar energy in H<sub>2</sub> production will play an essential role in solving the global energy crisis;<sup>[5]</sup> and since the first report of photocatalytic hydrogen generation by Fujishima and Honda,<sup>[6]</sup> solar-to-hydrogen energy conversion using photocatalysts has attracted great attention. Recently, H<sub>2</sub> production using a simple particulate photochemical system has shown great potential to achieve techno-economic viability.<sup>[7,8]</sup> For any particulate photochemical system, an efficient photocatalyst is the key feature

[\*] Dr. P. Sharma, Dr. M. Dearg, Dr. M. Wilding, Dr. T. J. A. Slater,  
Prof. C. R. A. Catlow  
School of Chemistry, Cardiff University  
Cardiff CF10 3AT (UK)  
E-mail: sharmap14@cardiff.ac.uk  
catlowr@cardiff.ac.uk

Dr. P. Sharma, Dr. M. Wilding, Prof. C. R. A. Catlow  
UK Catalysis Hub, Research Complex at Harwell, Rutherford  
Appleton Laboratory  
Harwell, OX11 0FA (UK)

Dr. M. Sharma  
Department of Chemistry, Kurukshetra University  
Kurukshetra 136119 (India)  
Prof. C. R. A. Catlow  
Department of Chemistry, University College London  
London WC1 HOAJ (UK)

© 2023 The Authors. Angewandte Chemie International Edition published by Wiley-VCH GmbH. This is an open access article under the terms of the Creative Commons Attribution License, which permits use, distribution and reproduction in any medium, provided the original work is properly cited.



**Scheme 1.** Cooperative coupling of solar H<sub>2</sub> generation and in situ synthesis of Pt single-atom anchored CdS<sub>15</sub> nanoparticles (Pt<sub>SA</sub>-CdS<sub>15</sub>) during photoirradiation. Schematic illustration highlighting the concurrent H<sub>2</sub> production and synthesis of Pt<sub>SA</sub>-CdS<sub>15</sub> semiconductors in a single photoinduced reaction system.

conductor heterostructures suitable for photochemical, and possible other applications.

## Results and Discussion

First, we tested the efficiency of the photoactive Cd<sub>x</sub>-Pt<sub>y</sub>-SSs reaction suspension, obtained by simple mixing of cadmium nitrate and chloroplatinic acid (Figure S1), for H<sub>2</sub> production under UV/Visible light illumination by using a continuous flow reaction setup connected to an online gas chromatograph (Figure S2). To study the synergistic effect of the presence of both metals in the suspension, the photoactivity of single metal precursor suspensions (Cd-SSs and Pt-SSs) were both examined (Figure S3). Next, the photoactivity of the reaction suspensions containing both the metal precursors (Cd<sub>x</sub>-Pt<sub>y</sub>-SSs,  $x=1$  mg in 15 mL SSs,  $y=0.5$  to 8.0 wt.% of  $x$ ) was analysed to determine the optimal amount of Pt, while keeping the amount of Cd constant in the suspension (Figure 1a). It was observed that the addition of Pt to the Cd-SSs suspension increases the H<sub>2</sub> production rate (Figures 1a and Figure S4). The presence of 2.0 wt.% Pt in the reaction suspension (Cd-Pt<sub>2</sub>-SSs) showed a 4.7 fold increase (154.7 mmol g<sup>-1</sup> h<sup>-1</sup>) in the H<sub>2</sub> production rate compared to Cd-SSs suspension. A further increase in Pt to 4 wt.% (Cd-Pt<sub>4</sub>-SSs) resulted in a maximum H<sub>2</sub> production rate of 166.7 mmol g<sup>-1</sup> h<sup>-1</sup>, whereas a decrease in H<sub>2</sub> production rate was observed for a reaction suspension containing 8 wt.% Pt (Cd-Pt<sub>8</sub>-SSs) (Figure 1a and Figure S4).

The Cd-SSs reaction suspension showed a high H<sub>2</sub> production rate (32.9 mmol g<sup>-1</sup> h<sup>-1</sup>) but the addition of Pt further increased the rate of H<sub>2</sub> production. We chose 2 wt.% Pt as the optimized Pt amount in suspension because

the increase in H<sub>2</sub> production above 2 wt.% Pt is relatively small (<10%) and Pt use should be minimized to provide low-cost H<sub>2</sub> production. Furthermore, Figure S5 shows the effect of the Cd content in the reaction suspension with 2 wt.% Pt (Cd<sub>x</sub>-Pt<sub>2</sub>-SSs,  $x=0.5, 1.0$  and 2.0 mg) on the H<sub>2</sub> production rate. Overall, 1 mg Cd to 15 mL of SSs and the addition of 2 wt.% Pt (Cd-Pt<sub>2</sub>-SSs) is considered the optimal reaction suspension for the present study.

Solar H<sub>2</sub> production of reaction suspensions of Cd-Pt<sub>2</sub>-SSs and Cd-SSs under UV/Visible light, measured using the continuous flow system, are illustrated in Figure 1b. The results obtained were compared with the H<sub>2</sub> production photoactivity of commercial CdS<sub>c</sub> and 2 wt.% Pt loaded commercial CdS<sub>c</sub> (Pt@CdS<sub>c</sub>) photocatalysts. The Cd-SSs and Cd-Pt<sub>2</sub>-SSs exhibited remarkably high H<sub>2</sub> production rates of 32.9 and 154.7 mmol g<sup>-1</sup> h<sup>-1</sup>, respectively (Figure 1b). In contrast, the commercial CdS<sub>c</sub> and Pt@CdS<sub>c</sub> produced very small amounts of H<sub>2</sub> that remain undetectable (Figure 1b) in the continuous flow system used. Therefore, to estimate the H<sub>2</sub> production from commercial CdS<sub>c</sub> and Pt@CdS<sub>c</sub>, an airtight cylindrical quartz reactor capped with rubber septa (Figure S1) was used under the same conditions by dispersing 1 mg of the photocatalyst in 15 mL SSs containing 2 wt.% Pt (relative to Cd metal). Before light irradiation, the precursor suspension was degassed by continuous purging of high purity Ar gas for 30 min in the dark to remove the dissolved gases. H<sub>2</sub> production using commercial CdS<sub>c</sub> and Pt@CdS<sub>c</sub> was then analysed by direct injection of gases collected from the headspace (16 mL) using a gas-tight syringe (injection volume of 250 μL) into the gas chromatograph. The Pt@CdS<sub>c</sub> showed a low H<sub>2</sub> production rate (0.214 mmol g<sup>-1</sup> h<sup>-1</sup>) (Figure 1c, and Figure S6). The observed H<sub>2</sub> production results using Cd-SSs, Cd-Pt<sub>2</sub>-SSs, and Pt@CdS<sub>c</sub> were further compared with previously reported photocatalytic H<sub>2</sub> production activity values of Pt-CdS<sub>R</sub> in Figure 1c.<sup>[25]</sup> It can be seen from Figure 1c that the Cd-Pt<sub>2</sub>-SSs reaction suspension demonstrated 723 times higher solar H<sub>2</sub> production than that of Pt@CdS<sub>c</sub> (0.214 mmol g<sup>-1</sup> h<sup>-1</sup>), and 736 times higher than the previously reported Pt-CdS<sub>R</sub> nanoparticulate systems (0.21 mmol g<sup>-1</sup> h<sup>-1</sup>).<sup>[25]</sup> Furthermore, even without using Pt, the Cd-SSs suspension produced 154 and 157-fold higher H<sub>2</sub> production rates than the Pt@CdS<sub>c</sub> and Pt-CdS<sub>R</sub> nanoparticles<sup>[25]</sup> (Figure 1c, Note S1), respectively. The real-time optical images of the solvent (SSs), single metal precursor suspensions (Cd-SSs), and Cd-Pt<sub>2</sub>-SSs reaction suspension before and after photoirradiation are shown in Figure S7.

We checked the influence of the excitation wavelength on H<sub>2</sub> production using the Cd-Pt<sub>2</sub>-SSs reaction suspension for 4 different cut-off wavelengths (Figure 1d). These results firmly supported the operational viability under visible light illumination. The recorded video (Movie S1) highlighted the release of H<sub>2</sub> bubbles from the settled down Cd-Pt<sub>2</sub>-SSs reaction suspension in a glass test tube on irradiation with 365 nm LED light. The solar H<sub>2</sub>-production rates of the Cd-Pt<sub>2</sub>-SSs reaction suspension under UV/Visible light irradiation can be well maintained during repeated (Figure 1e) and long-term (Figure S8) stability tests. The relatively small decrease in H<sub>2</sub> production during the photocatalytic cycles is

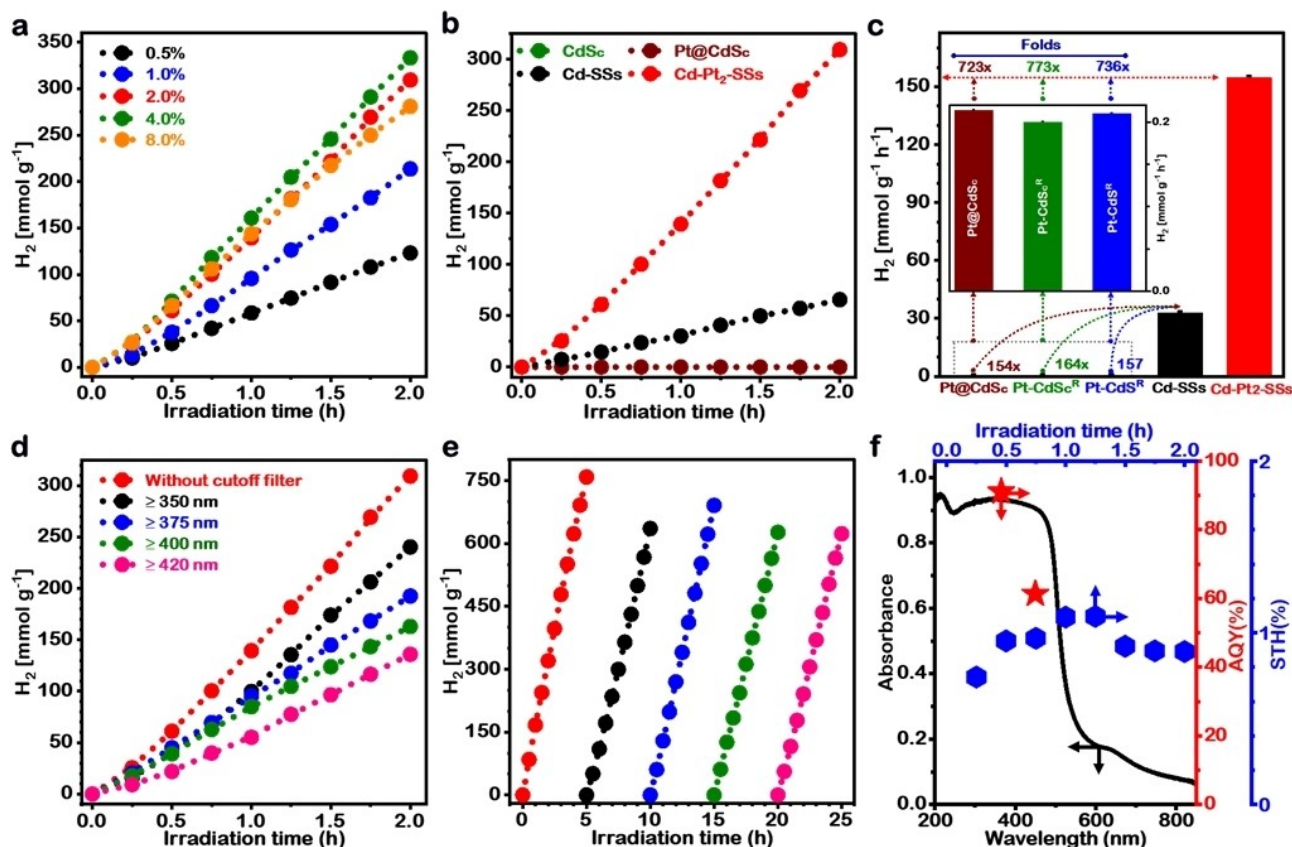


**Figure 1.** Photochemical  $\text{H}_2$  production performance of  $\text{Cd}_x\text{Pt}_y\text{-SSs}$ . a,  $\text{H}_2$  production time profile for mixed metals precursors suspension,  $\text{Cd}_x\text{Pt}_y\text{-SSs}$  ( $x=1$  mg in 15 mL SSs,  $y=0.5$  to 8.0 wt.% Pt of  $x$ ). b, Comparison of  $\text{H}_2$  production time profiles of  $\text{Cd-SSs}$  and  $\text{Cd-Pt}_2\text{-SSs}$  with commercial  $\text{CdSc}$  and 2%Pt@ $\text{CdSc}$ . (Note:  $\text{H}_2$  production profile of commercial 2%Pt@ $\text{CdSc}$  overlaps with that of  $\text{CdSc}$ .) c,  $\text{H}_2$  production rate over commercial  $\text{CdSc}$  (this study), commercial  $\text{CdS}$  reported in the referred paper ( $\text{CdSc}^R$ ), and  $\text{CdS}$  nanoparticles ( $\text{CdS}^R$ ) reported by Bag et al.<sup>[25]</sup> (inset magnified bar graph), and a comparison with  $\text{Cd-SSs}$  and  $\text{Cd-Pt}_2\text{-SSs}$  reaction suspension. d, Time profile of  $\text{H}_2$  production from  $\text{Cd-Pt}_2\text{-SSs}$  at different cut-off wavelengths. e, Repeated run stability analysis of  $\text{Cd-Pt}_2\text{-SSs}$ . f, Apparent quantum yield as a function of the incident light wavelength, and time profile of solar to hydrogen conversion efficiency ( $2\text{H}^+ + 2\text{e}^- \rightarrow \text{H}_2$ ).

probably due to modifications in the nearby coordination environments of active sites and some structural changes in the photocatalysts. The stability of the solid material collected from  $\text{Cd-Pt}_2\text{-SSs}$  reaction suspension after the 5<sup>th</sup> run of cyclic stability test has been analysed by UV/Vis absorbance (Figure S9), Raman (Figure S10), Fourier transform infrared (FTIR) (Figure S11), and  $\text{N}_2$  adsorption-desorption (Figure S12) analyses. All these studies further confirm the structural stability of the photocatalytic system. Also, to check the possibility of any photo-chemical corrosion of in situ generated  $\text{Pt}_{\text{SA}}\text{-CdS}_{\text{IS}}$ , microwave plasma-atomic emission spectroscopy (MP-AES) (Figures S13 and S14) has been used; however, the obtained results indicate the complete absence of Cd and Pt in the solution phase. A high AQY ( $\approx 91.1\%$  (365 nm), and 61.3% (450 nm)), and solar-to-hydrogen conversion efficiency, ( $\eta \approx 1.0\%$ ) were achieved in the presence of an electron donor (Figure 1f).

The reaction suspensions ( $\text{Cd-Pt}_2\text{-SSs}$  and  $\text{Cd-SSs}$ ) used in the present study were compared with  $\text{H}_2$  generating photocatalysts (co-catalyst loaded metal oxide, metal sulphide, carbon-based, metal-organic framework (MOF)

based, and MOF-metal-carbon (MOF-M-C) photocatalysts) discussed in previous work (Table S1).<sup>[21,26-30]</sup> Our reported suspensions, which do not require any pre-synthesis, show comparable  $\text{H}_2$  production to the previously reported photocatalysts, which require a multistep synthesis process, high-cost organic solvents, sophisticated reaction setup, additional thermal treatments, and co-catalyst loading. We note that even the Pt-free,  $\text{Cd-SSs}$  reaction suspension showed remarkable  $\text{H}_2$  production that is comparable to that of single-atom metal catalyst loaded  $\text{TiO}_2$ ,  $\text{CdS}$ , and  $\text{g-C}_3\text{N}_4$  photocatalysts. In short, the direct use of metal precursor solutions may prove to be a novel, promising, environmentally benign, and cost-effective strategy for effective  $\text{H}_2$  production.

Several studies have reported the effect of solar radiation on the surface structure of photocatalysts during photochemical reactions.<sup>[31-34]</sup> To explore the driving force behind the exceptional photochemical  $\text{H}_2$  production performances of  $\text{Cd-SSs}$  and  $\text{Cd-Pt}_2\text{-SSs}$  suspensions, the chemical, electrochemical, optical, electronic, and structural characteristics of the suspended nanoparticles generated during solar  $\text{H}_2$  production were extensively investigated. X-

ray diffraction (Figure S15) and high-angle annular dark-field scanning transmission electron microscopy (HAADF-STEM) (Figure 2a–c and Figure S16) indicated a mixture of the zincblende and wurtzite structures for in situ synthesized CdS<sub>IS</sub> nanoparticles in Cd-SSs suspension by photoirradiation during solar H<sub>2</sub> production. Fourier transforms of the data taken from two different nanoparticles in Figure 2a demonstrate the presence of both wurtzite and zincblende structures in close proximity.

As discussed earlier, the addition of a small weight percentage of the Pt precursor (2 wt.% of Cd) to the Cd-SSs suspension results in a nearly 4.7 fold higher H<sub>2</sub> production

than the H<sub>2</sub> production from the Cd-SSs suspension without Pt (Figure S4). We examined the Cd-Pt<sub>2</sub>-SSs suspension after solar H<sub>2</sub> production to determine the nature of Pt in the system. HAADF-STEM images (Figure 2d and Figure S17) demonstrated the in situ formation of isolated Pt single-atoms anchored on the CdS nanoparticles (Pt<sub>SA</sub>-CdS<sub>IS</sub>) without any noticeable atom assemblies (two-dimensional “rafts” of Pt atoms) after solar H<sub>2</sub> production. However, elemental mapping using energy dispersive X-ray (EDX) spectroscopy found the presence of small nanoparticles of Pt, in addition to the single atoms (Figure 2e–h). Pt could be observed on Cd-Pt<sub>2</sub>-SSs in regions without

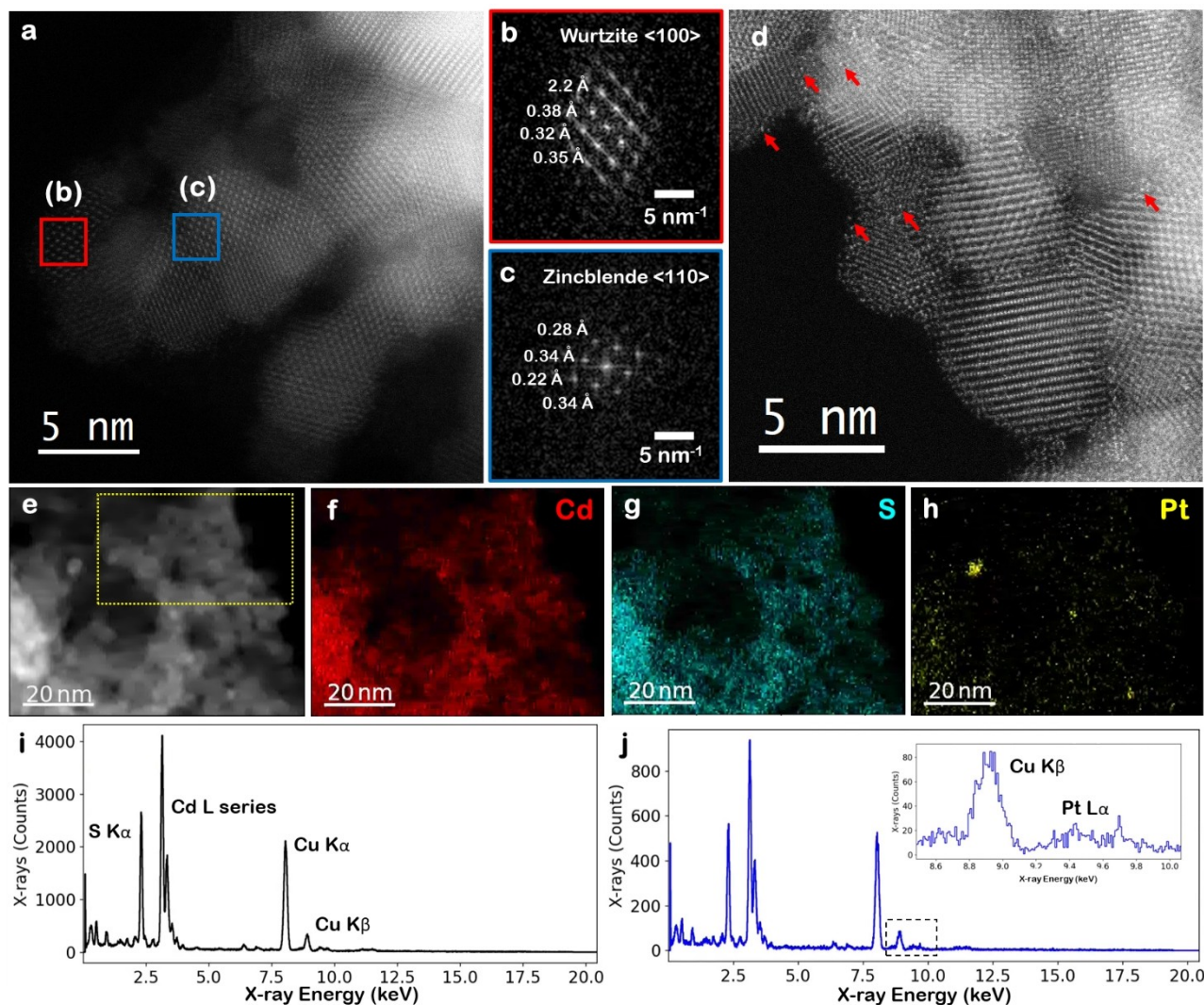


**Figure 2.** Structural evolution of photoinduced in situ synthesised Pt single-atoms anchored CdS<sub>IS</sub> semiconductor. a, HAADF-STEM image demonstrating the atomic structure of CdS<sub>IS</sub> particles. b, The Fourier Transform of the region indicated in (a), which is indexed to a  $\langle 100 \rangle$  direction in wurtzite CdS. c, The Fourier Transform of the region indicated in (a), which is indexed to a  $\langle 110 \rangle$  direction in zincblende CdS. d, HAADF-STEM image in which bright atoms (Pt) can be observed in addition to CdS<sub>IS</sub> particles. A selection of bright atoms has been highlighted with red arrows. e, HAADF-STEM image of a region corresponding to the EDX maps in f–h, where the dashed yellow box indicates the region in which spectrum j has been extracted. f–h, Corresponding EDX maps of the full region for Cd (f), S (g), and Pt (h). Small Pt single-atom clusters can be observed in the Pt map. i, Sum EDX spectrum taken from the whole region shown in Figure 2e. Clear Cd and S peaks can be seen. j, EDX spectrum taken solely from the region highlighted in yellow dotted rectangle Figure 2e, in which there are no clear Pt nanoparticles. All peaks remain, including the Pt L peaks. Inset is a highlighted region of the spectrum specifically highlighting the presence of a small Pt L $\alpha$  peak at 9.44 keV.

visible nanoparticles (Figure 2j), confirming the presence of single atoms or small clusters, which we suggest are single atoms based on the HAADF-STEM imaging conducted. On the other hand, the Cd-SSs suspension with 8 wt.% Pt showed the presence of Pt atom assemblies, along with well distributed Pt single-atoms on the CdS nanoparticles in the Cd-Pt<sub>8</sub>-SSs suspension after solar H<sub>2</sub> production (Figure S18). The observed decrease in the H<sub>2</sub> production rate (Figure S4) for the Cd-Pt<sub>8</sub>-SSs suspension can be expected because high Pt loading (8 wt.%) on CdS<sub>15</sub> nanoparticles can limit the radiation exposure of the CdS<sub>15</sub> nanoparticles and diminish the surface sites for the adsorption of the sacrificial agent (SSs).<sup>[35]</sup> Thus, we have achieved the in situ synthesis of isolated Pt single-atom anchored CdS nanoparticles (Pt<sub>SA</sub>-CdS<sub>15</sub>) without requiring any separate synthesis process. More importantly, loading single-atom metal co-catalysts higher than 0.5 wt.% is very challenging and typically requires a complex synthesis process;<sup>[26,36–39]</sup> our approach yielded a highly dispersed distribution of Pt single-atoms anchored on CdS<sub>15</sub> along with solar H<sub>2</sub> production. A high

atomic dispersion of Pt single-atoms anchored on CdS<sub>15</sub> nanoparticles offers robust catalytic activity, unique selectivity, and effective photoactive charge carrier utilization for photochemical H<sub>2</sub> production.<sup>[40]</sup>

Ex situ X-ray photoelectron spectroscopy (XPS) analysis was performed to determine the surface chemical composition and oxidation states of Cd and Pt in powder samples collected from Cd<sub>x</sub>-Pt<sub>y</sub>-SSs (x = 1 mg 15 mL<sup>-1</sup>, y = 0, 2, 4 and 8 % of x) suspensions before and after solar H<sub>2</sub> production. The spectra of samples collected from Cd-Pt<sub>2</sub>-SSs suspensions before photoirradiation showed the presence of Cd 3d and S 2p only (Figure S19). However, the spectra of powder samples collected from Cd-Pt<sub>y</sub>-SSs suspensions after photoirradiation exhibit the presence of Cd 3d, S 2p, and Pt 4f signals (Figures 3a–d, S20–S22, and Tables S2–S4). These results demonstrate that simultaneous in situ photodeposition of Pt does not occur without UV/Visible light irradiation. In fact, it confirms the facile synthesis of a photo-induced Pt<sub>SA</sub>-CdS<sub>15</sub> (Figures 2a, 3d, S17, S18, S21, S22)

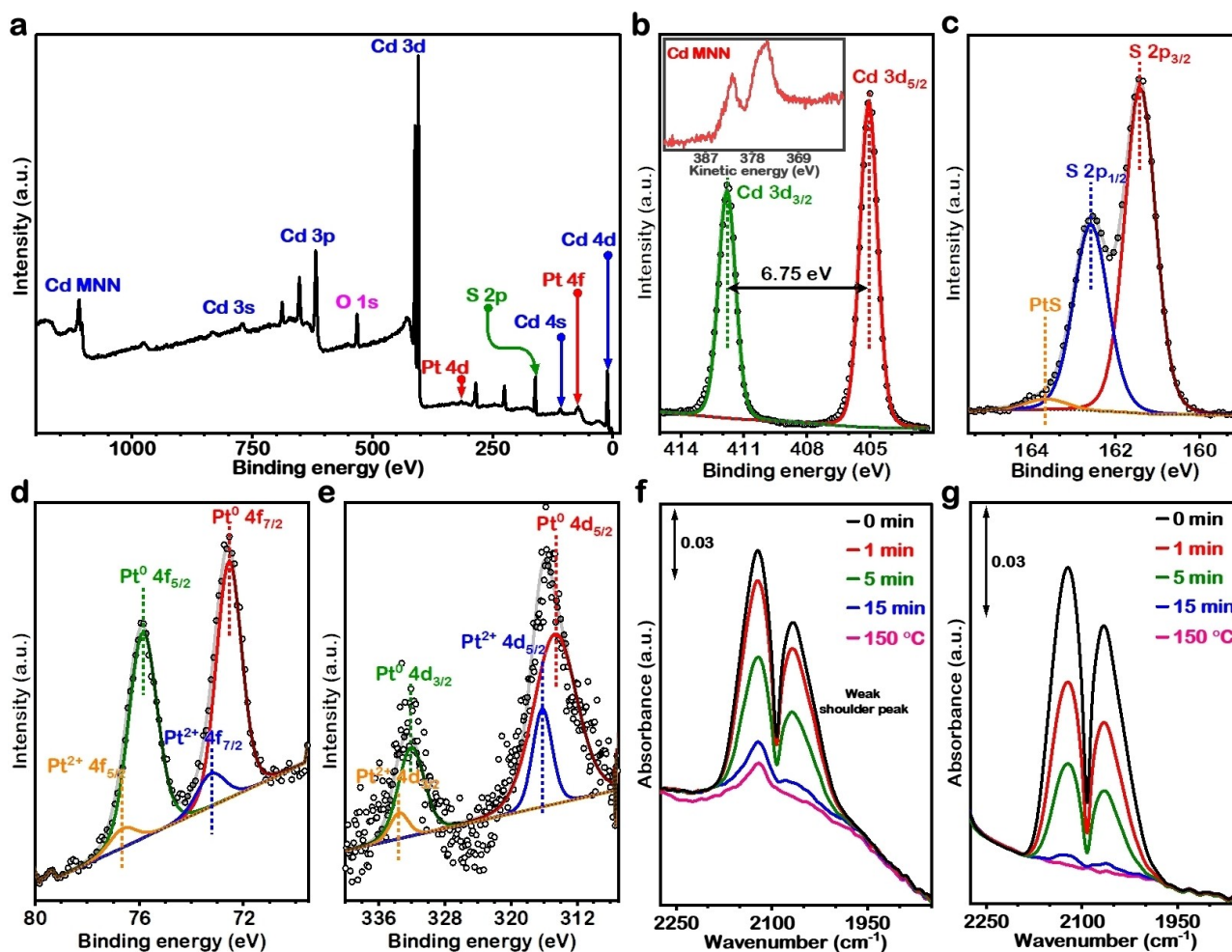


**Figure 3.** Electronic state identification of atomically dispersed Pt atoms over an in situ generated Pt<sub>SA</sub>-CdS<sub>15</sub> photocatalyst. a, Overall XPS survey spectrum of Pt<sub>SA</sub>-CdS<sub>15</sub> (2 wt.% Pt of Cd). b, High-resolution XPS spectra of Cd 3d, Cd MNN (inset spectrum) and c, S 2p for Pt<sub>SA</sub>-CdS<sub>15</sub> photocatalyst. Deconvolution of the high-resolution XPS peaks for d, Pt 4f and e, Pt 4d showing the presence of Pt<sup>0</sup> single atoms. Time-dependent FTIR spectra of CO adsorbed at 293 K (0 min) followed by desorption using He gas purging (20 cc min<sup>-1</sup>) and thermal treatment at 150 °C, 30 min for f, Pt<sub>SA</sub>-CdS<sub>15</sub> and g, commercial 5%Pt/Al<sub>2</sub>O<sub>3</sub> samples.

alongside H<sub>2</sub> production (Figure 1) from Cd-Pt<sub>y</sub>-SSs suspensions.

The high-resolution X-ray photoemission spectrum of the Cd 3d peaks (Figure 3b) showed Cd 3d<sub>3/2</sub> (411.7 eV) and Cd 3d<sub>5/2</sub> (405.0 eV) peaks, which correspond to the characteristic peak of the Cd<sup>2+</sup> oxidation state of CdS<sub>IS</sub>. The characteristic binding energies states of S 2p<sub>1/2</sub> (162.5 eV) and S 2p<sub>3/2</sub> (161.4 eV) are determined by deconvoluting them from the main S 2p peak in Figure 3c. The observed peaks of the S 2p states confirm the presence of S<sup>2-</sup> in the Pt<sub>SA</sub>-CdS<sub>IS</sub>.

The high-resolution XPS spectra for Pt 4f (Figure 3d) indicated two kinds of platinum species<sup>[41]</sup> with a small change in the binding energies of Pt 4f<sub>7/2</sub> and Pt 4f<sub>5/2</sub>.<sup>[42]</sup> Deconvolution analysis revealed the peaks at 72.3 and 75.6 eV with a spin-orbit split of 3.3 eV, indicating the presence of Pt<sup>0</sup>, while the peaks at 73.4 and 76.7 eV can be assigned to Pt<sup>2+</sup>.<sup>[43,44]</sup> The higher Pt<sup>0</sup> binding energy in Pt<sub>SA</sub>-CdS<sub>IS</sub> (72.3 eV) than the standard 71.8 eV suggests stronger electronic interaction between Pt<sub>SA</sub> and CdS<sub>IS</sub>. The presence of the well-contacted interface between Pt<sub>SA</sub> and CdS<sub>IS</sub> enhances electron mobility across the interface and reduces the energy barriers for H<sub>2</sub> evolution.<sup>[45,46]</sup>

The atomic ratio Pt<sup>0</sup>:Pt<sup>2+</sup> was estimated to be high, with Pt largely dispersed as single-atom species in the in situ synthesized Pt<sub>SA</sub>-CdS<sub>IS</sub> photocatalyst irrespective of initial Pt content (Tables S2–S4). Furthermore, the deconvolution of

Pt 4d XPS peaks also confirms the predominance of charge-neutral Pt in the Pt<sub>SA</sub>-CdS<sub>IS</sub> photocatalyst (Figure 3e).<sup>[47]</sup>

Site-specific analysis using CO adsorption infrared spectroscopy (Figures 3f, and 3g) was performed to supplement the HAADF-STEM and XPS results and to provide complementary information about the distribution of metallic platinum and the presence of Pt<sup>0</sup> state in the Pt<sub>SA</sub>-CdS<sub>IS</sub> sample. The IR absorbance spectra of adsorbed CO on Pt<sub>SA</sub>-CdS<sub>IS</sub> showed two strong vibration bands and a weak shoulder peak (Figure 3f). These peaks probably originate from CO molecules adsorbed on different metal species.<sup>[48–50]</sup> Furthermore, 5 wt.% metallic Pt loaded Al<sub>2</sub>O<sub>3</sub> (5%Pt/Al<sub>2</sub>O<sub>3</sub>) was used as a reference CO adsorption study. The CO adsorption IR spectra for commercial 5%Pt/Al<sub>2</sub>O<sub>3</sub> (Figure 3g) are similar to that of Pt<sub>SA</sub>-CdS<sub>IS</sub>, and are the subject of further studies.

The electronic and coordination structures of Pt species in Pt<sub>SA</sub>-CdS<sub>IS</sub> photocatalyst were further validated by X-ray absorption near-edge structure (XANES) and extended X-ray absorption fine structure (EXAFS) analysis in comparison to Pt foil and PtO<sub>2</sub> references. The normalised XANES spectra reported in Figure 4a show that white line edge intensity of Pt species in Pt<sub>SA</sub>-CdS<sub>IS</sub> is much lower than that of PtO<sub>2</sub> (Pt<sup>4+</sup>) and very close to the Pt foil (Pt<sup>0</sup>) reference, which confirms the existence of Pt species as single atoms in the in situ generated Pt<sub>SA</sub>-CdS<sub>IS</sub> photocatalyst, which is consistent with the HAADF-STEM (Figure 2), XPS (Figure 3a–e), and site-specific CO adsorption FTIR (Fig-

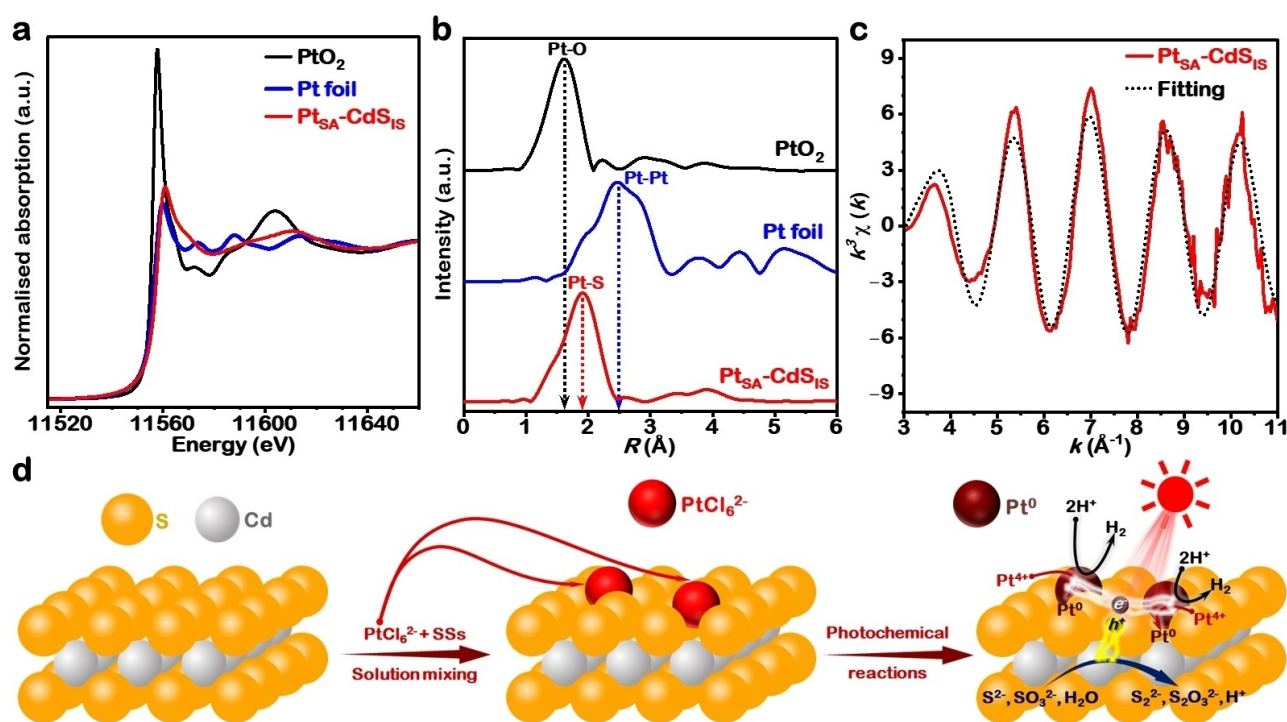


**Figure 4.** X-ray absorption fine structure (XAFS) measurement of Pt<sub>SA</sub>-CdS<sub>IS</sub>. a, Normalised XANES spectra of Pt<sub>SA</sub>-CdS<sub>IS</sub>, and reference samples (PtO<sub>2</sub> and Pt foil) at the Pt L<sub>3</sub> edge. b, Fourier transformed (FT)  $k^3$ -weighted  $\chi(k)$  function of the EXAFS spectra of Pt<sub>SA</sub>-CdS<sub>IS</sub>, PtO<sub>2</sub> and Pt foil. c, Corresponding EXAFS fitting curve of Pt<sub>SA</sub>-CdS<sub>IS</sub> at  $k$ . d, Possible photochemical parallel reduction reactions resulting in H<sub>2</sub> production and synthesis of Pt single-atom decorated CdS<sub>IS</sub> semiconductor. The electron charge sharing helps in high H<sub>2</sub> production and high yield of single atom Pt<sup>0</sup>.

ure 3f,g) results. As shown in Figure 4b, the presence of a prominent peak at  $1.91 \text{ \AA}$  attributed to the Pt–S coordination<sup>[49,51,52]</sup> and the absence of Pt–O ( $\approx 1.63 \text{ \AA}$ ) and Pt–Pt coordination ( $\approx 2.5\text{--}2.8 \text{ \AA}$ ) peaks in the EXAFS spectrum of Pt<sub>SA</sub>-CdS<sub>IS</sub>, and the corresponding best-fitting to the data (Figure 4c) reinforce the conclusion that Pt remained atomically dispersed on in situ generated CdS<sub>IS</sub>.<sup>[51–54]</sup> Thus, Figure 4d illustrates the occurrence of two parallel reactions: H<sub>2</sub> production and in situ formation of Pt single-atoms anchored CdS nanoparticles (Pt<sub>SA</sub>-CdS<sub>IS</sub>).

The UV–Vis absorbance spectra of the photoinduced in situ generated CdS<sub>IS</sub>, and Pt<sub>SA</sub>-CdS<sub>IS</sub> are reported in Fig-

ure 5a. We find that both the samples exhibited significant light absorption in the visible-light region. A small absorption band in the visible light region (550–700 nm) for Pt<sub>SA</sub>-CdS<sub>IS</sub> can be attributed to H<sub>2</sub> evolving platinum species. The band-gap energies ( $E_{BG}$ ) calculated using the Kubelka–Munk function,  $(F(R)h\nu)^2 = h\nu$ , (Figure 5a inset) for Pt<sub>SA</sub>-CdS<sub>IS</sub> (2.43 eV) and CdS<sub>IS</sub> (2.46 eV) are relatively similar and confirm that they can act as visible light absorbing photocatalysts.

The photochemical performance of a photocatalyst also depends on the conduction band (CB) and valence band (VB) positions, which were calculated following the method

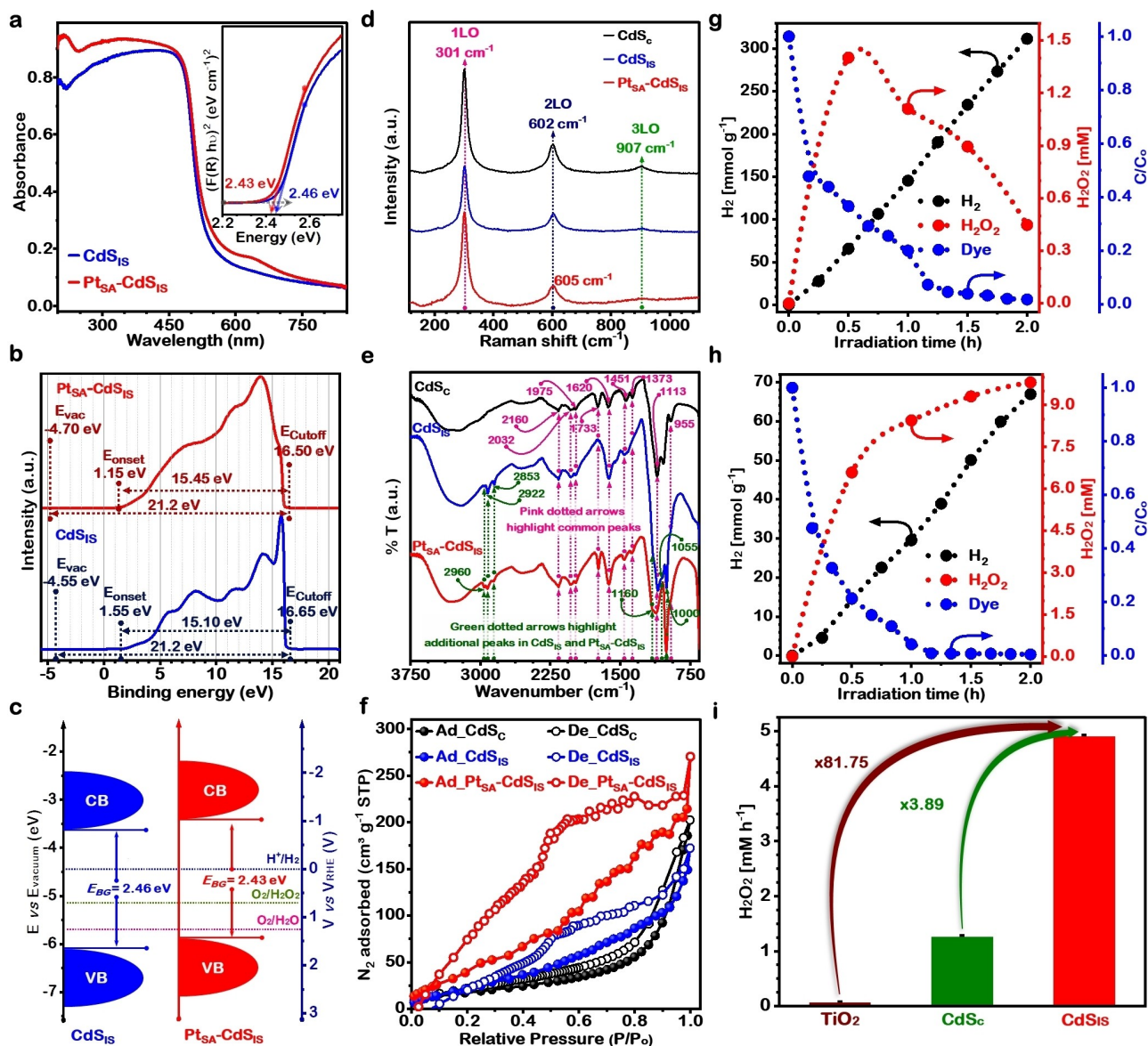


**Figure 5.** Electronic, physicochemical, and photochemical analysis of in situ generated Pt<sub>SA</sub>-CdS<sub>IS</sub> and CdS<sub>IS</sub>. a, Solid-state UV/Vis absorbance spectra and Kubelka–Munk plot (inset) for the band gap calculation. b, UPS spectra of CdS<sub>IS</sub> and Pt<sub>SA</sub>-CdS<sub>IS</sub>. c, Schematic of band gap and energy level bands with respect to vacuum level and reversible hydrogen electrode (RHE). d, Raman spectra, e, ATR-FTIR spectra, and f, N<sub>2</sub> adsorption-desorption isotherms for CdS<sub>IS</sub> and Pt<sub>SA</sub>-CdS<sub>IS</sub> photocatalysts. Solar H<sub>2</sub> production, O<sub>2</sub> reduction to H<sub>2</sub>O<sub>2</sub>, and dye degradation performance of g, Pt<sub>SA</sub>-CdS<sub>IS</sub> and h, CdS<sub>IS</sub>. i, A comparison of H<sub>2</sub>O<sub>2</sub> production rate over commercial CdS (CdS<sub>C</sub>, 98% Alfa Aesar), commercial TiO<sub>2</sub>, and as-synthesized CdS<sub>IS</sub> nanoparticles.

reported by Liu et al.<sup>[14]</sup> The valence band maximum for the respective photocatalysts was calculated by estimating the ionization potential (equivalent to the valence band energy ( $E_{\text{VB}}$ )) by subtracting the width of the He I UPS spectrum (Figure 5b) from the excitation energy (21.2 eV). The relative  $E_{\text{VB}}$  are calculated to be  $-6.10$  eV ( $\text{CdS}_{\text{IS}}$ ) and  $-5.85$  eV ( $\text{Pt}_{\text{SA}}\text{-CdS}_{\text{IS}}$ ) compared with  $E_{\text{vacuum}}$  according to UPS spectra (Figure 5b and c). Using the  $E_{\text{BG}}$  values the CB edge/energy ( $E_{\text{CB}}$ ) of  $\text{CdS}_{\text{IS}}$  and  $\text{Pt}_{\text{SA}}\text{-CdS}_{\text{IS}}$  have been estimated to be  $-3.64$  eV, and  $-3.42$  eV, respectively (Figure 5c).

Raman (Figure 5d) and FTIR (Figure 5e) spectra confirmed the in situ crystallization of  $\text{CdS}_{\text{IS}}$ . Raman spectra, as presented in Figure 5d, reveal the strongest peaks at  $301\text{ cm}^{-1}$ , which is due to first-order longitudinal optical (LO) phonons, and second-order LO (2LO) occurring at  $\approx 602\text{ cm}^{-1}$  identified as characteristic peaks for  $\text{CdS}$ .<sup>[55]</sup> In comparison with  $\text{CdS}_{\text{IS}}$ , these peaks are relatively intense for  $\text{Pt}_{\text{SA}}\text{-CdS}_{\text{IS}}$ , suggesting possible electric field enhancement over the  $\text{CdS}_{\text{IS}}$  surface.<sup>[56]</sup> The photoluminescence (PL) emission spectra for  $\text{CdS}_{\text{c}}$ ,  $\text{CdS}_{\text{IS}}$ , and  $\text{Pt}_{\text{SA}}\text{-CdS}_{\text{IS}}$  recorded at an excitation wavelength of 450 nm (Figure S23) provide information about the effective separation of photogenerated charge carriers. Figure S23 highlights the suppressed electron-hole pair recombination rate and enhanced charge carrier separation efficiency of  $\text{CdS}_{\text{IS}}$ , and  $\text{Pt}_{\text{SA}}\text{-CdS}_{\text{IS}}$  relative to commercial  $\text{CdS}_{\text{c}}$ .

To explore the textural properties, and to study the porous character of  $\text{CdS}_{\text{IS}}$  and  $\text{Pt}_{\text{SA}}\text{-CdS}_{\text{IS}}$  nanoparticles,  $\text{N}_2$  adsorption-desorption measurements were performed at 77 K (Figure 5f, and Table S5). Furthermore, a comparison of the textural properties of  $\text{Pt}_{\text{SA}}\text{-CdS}_{\text{IS}}$  nanoparticles with commercial  $\text{CdS}_{\text{c}}$  (Figure 5f, Table S5) highlights a larger BET-specific surface area ( $S_{\text{BET}}$ ) of  $151.3\text{ m}^2\text{ g}^{-1}$  owing to the nanostructure of  $\text{CdS}_{\text{IS}}$ , the relatively higher porosity/mesoporous character, and atomically decorated  $\text{Pt}_{\text{SA}}$ , whereas the  $\text{CdS}_{\text{c}}$  particles have a lower  $S_{\text{BET}}$  ( $62.85\text{ m}^2\text{ g}^{-1}$ ). The nanostructure of  $\text{Pt}_{\text{SA}}\text{-CdS}_{\text{IS}}$  which arises from the photoinduced controlled crystallization might contribute to the improved surface structure and light-harvesting efficiency.

The photochemical performance of both in situ generated visible-light absorbers has been comprehensively investigated under UV/Visible light for  $\text{H}_2$  evolution,  $\text{H}_2\text{O}_2$  production, and dye degradation (Figures 5g, 5h and Figures S24 and S25). The  $\text{H}_2$  and  $\text{H}_2\text{O}_2$  production profiles, and alizarin red S (ARS) dye degradation over time for  $\text{Pt}_{\text{SA}}\text{-CdS}_{\text{IS}}$  and  $\text{CdS}_{\text{IS}}$  photocatalysts are reported in Figure 5g and Figure 5h, respectively. As expected, the solar  $\text{H}_2$  production over these two photocatalysts  $\text{Pt}_{\text{SA}}\text{-CdS}_{\text{IS}}$  and  $\text{CdS}_{\text{IS}}$  is similar to the photochemical  $\text{H}_2$  production performance of their mother liquids  $\text{Cd-Pt}_2\text{-SSs}$  and  $\text{Cd-SSs}$ , respectively. Interestingly, a record high solar  $\text{H}_2\text{O}_2$  production of  $4.91\text{ mMh}^{-1}$  was recorded for  $\text{CdS}_{\text{IS}}$  in  $\text{O}_2$  saturated 10 M ethanol solution (Figure 5h). In contrast, commercial  $\text{CdS}_{\text{c}}$  (Figure S26) and  $\text{TiO}_2$  (Figure S27) photocatalysts show low solar  $\text{H}_2\text{O}_2$  production under the same experimental conditions compared to that of  $\text{CdS}_{\text{IS}}$  (Figure 5i). Furthermore, a comparison was made with previously

reported photocatalysts for similar reaction systems, and  $\text{CdS}_{\text{IS}}$  shows a comparable solar  $\text{H}_2\text{O}_2$  production rate (Table S6).

In this study, we report the successful synthesis of transparent  $\text{Pt}_{\text{SA}}\text{-CdS}_{\text{IS}}$  and  $\text{CdS}_{\text{IS}}$  films having exceptional photocatalytic activity and good PEC performance.  $\text{Pt}_{\text{SA}}\text{-CdS}_{\text{IS}}$ ,  $\text{CdS}_{\text{IS}}$ , and  $\text{CdS}_{\text{c}}$  films were fabricated by a simple drop-casting method on a fluorine-doped tin oxide (FTO) glass substrate and were subsequently dried at room temperature followed by vacuum drying. The top view SEM images (Figures 6a, and b) and digital photographs (inset images) of the  $\text{Pt}_{\text{SA}}\text{-CdS}_{\text{IS}}$  and  $\text{CdS}_{\text{IS}}$  films demonstrate a uniform and transparent film formation on the FTO substrate.

To investigate the interfacial charge separation and transport behaviour of the samples ( $\text{Pt}_{\text{SA}}\text{-CdS}_{\text{IS}}$ ,  $\text{CdS}_{\text{IS}}$  and  $\text{CdS}_{\text{c}}$ ), electrochemical impedance spectroscopy (EIS) measurements were conducted under light irradiation and dark conditions. Nyquist plots shown in Figure 6c demonstrated that a smaller arc radius was observed for  $\text{Pt}_{\text{SA}}\text{-CdS}_{\text{IS}}$  both in the dark and under illumination as compared to those of  $\text{CdS}_{\text{IS}}$  and  $\text{CdS}_{\text{c}}$ . As arcs in the Nyquist plot reflect charge-transfer resistance at the electrode surface, so a smaller arc radius indicates a fast interfacial charge transfer and an effective separation of the photogenerated electron-hole pairs in  $\text{Pt}_{\text{SA}}\text{-CdS}_{\text{IS}}$ . Furthermore, the photocurrent density-potential profiles shown in Figure 6d demonstrated the PEC performance of  $\text{Pt}_{\text{SA}}\text{-CdS}_{\text{IS}}$ ,  $\text{CdS}_{\text{IS}}$  and  $\text{CdS}_{\text{c}}$  photoanode from water oxidation via front illumination. These results clearly show a higher photocurrent response for  $\text{Pt}_{\text{SA}}\text{-CdS}_{\text{IS}}$  which complements the EIS results that a reduction in recombination of electron-hole pairs increases electron mobility.

To provide further information about the kinetics and electron transfer number ( $n$ ) involved in the oxygen reduction reaction for  $\text{H}_2\text{O}_2$  production (Figure 5h), we performed linear sweep voltammetry (LSV) experiments in oxygen saturated 0.1 M KOH solution (Figure 6e, and Figure S28a, and S29a). The current curves of the steady-state diffusion platform analyzed by the Koutecky-Levich (K-L) equation and the linearly fitted K-L plots for  $\text{CdS}_{\text{IS}}$ ,  $\text{Pt}_{\text{SA}}\text{-CdS}_{\text{IS}}$  and  $\text{CdS}_{\text{c}}$  are reported in Figure 6f, Figures S28b, and S29b, respectively. The slope of these K-L plots was utilised to evaluate the overall electron transfer number for the ORR. The estimated electron participation in ORR corresponding to different potentials in Figure 6g shows that the average value of  $n$  is 1.96 for  $\text{CdS}_{\text{IS}}$ , confirming the selective two-electron ORR pathway to the  $\text{H}_2\text{O}_2$  production over its surface.

## Conclusion

In contrast to the usual requirement of pre-synthesized photocatalysts for  $\text{H}_2$  production, we have demonstrated a proof-of-concept involving the direct use of metal (Cd and Pt) precursors in (sodium sulphide + sodium sulphite) solution as a UV/Visible light photocatalytic system and achieved significant photocatalytic  $\text{H}_2$  production activity ( $154.7\text{ mmol g}^{-1}\text{ h}^{-1}$   $\text{Cd-Pt}_2\text{-SSs}$ ), with an apparent quantum



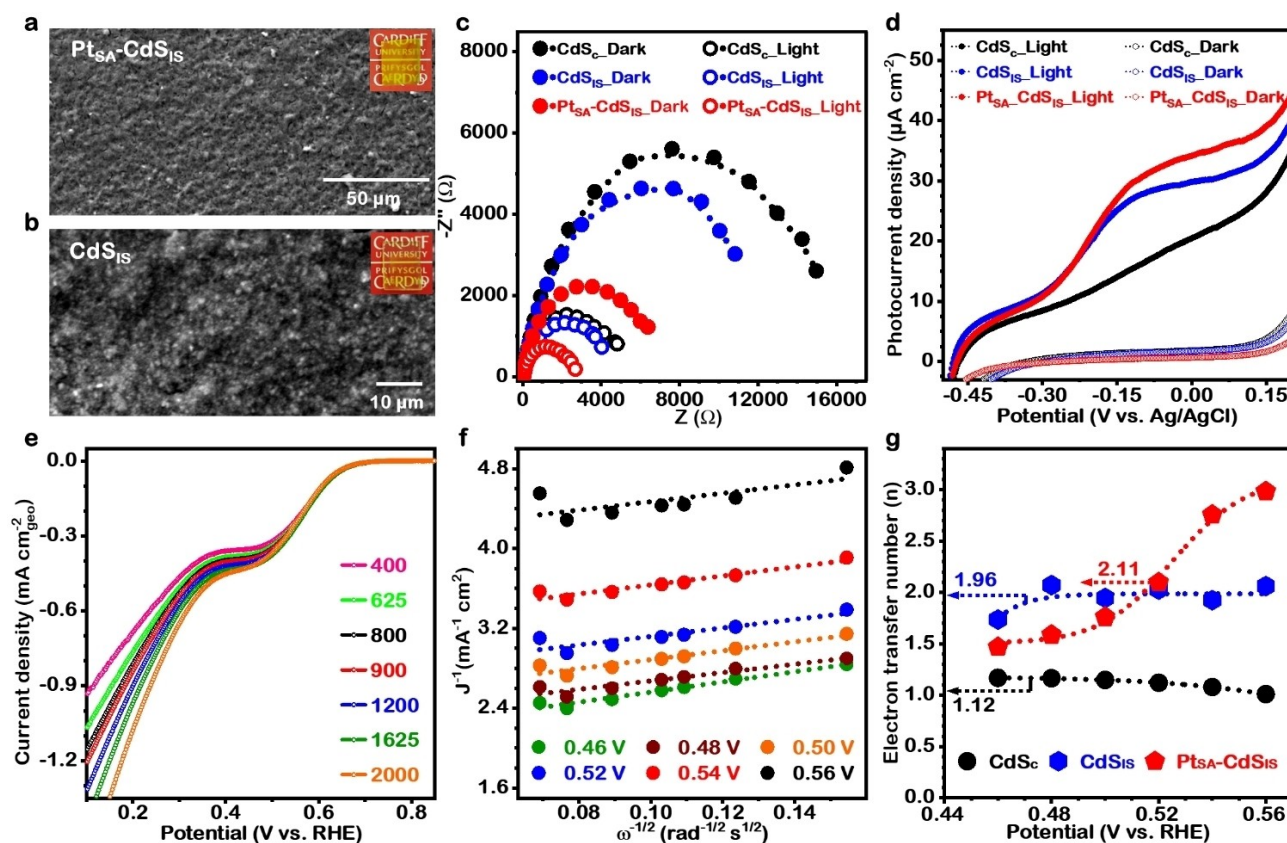


**Figure 6.** Photo-electrochemical performance. Top-view SEM image of drop cast a, Pt<sub>SA</sub>-CdS<sub>IS</sub> and b, CdS<sub>IS</sub> film on conductive FTO substrate. Inset digital photographs highlight the transparency of photoanodes. c, EIS Nyquist plots, and d, Photocurrent density-potential profile of Pt<sub>SA</sub>-CdS<sub>IS</sub>, CdS<sub>IS</sub>, and CdS<sub>c</sub>. e, Linear sweep voltammetry (LSV) of CdS<sub>IS</sub> in O<sub>2</sub> saturated 0.1 M KOH (pH 13) at different rotating speeds ranging from 400–2500 rpm and a fixed scanning rate of 5 mV s<sup>-1</sup>. f, Koutecky–Levich (K–L) plots of CdS<sub>IS</sub> at different potentials. g, The evaluated number of electrons participating in the ORR at corresponding potentials for CdS<sub>c</sub>, CdS<sub>IS</sub>, and Pt<sub>SA</sub>-CdS<sub>IS</sub> photocatalysts.

yield of over 91% which outperforms previously reported photochemical particulate systems. More importantly, we have observed simultaneous photoinduced in situ synthesis of Pt single-atom anchored on CdS nanoparticles (Pt<sub>SA</sub>-CdS<sub>IS</sub>) without utilizing any functionalized organic solvents. We suggest the junction formed between Pt<sub>SA</sub> and CdS<sub>IS</sub>, and the excellent H<sub>2</sub> activation property of Pt are responsible for the enhanced photocatalytic activity. So, the synergistic roles of Pt and CdS lead to it being more favourable for transferring photoexcited electrons (e<sup>-</sup>) to Pt, while Pt<sub>SA</sub> ensures outstanding e<sup>-</sup> mobility and offers more active sites for reducing H<sup>+</sup> to H<sub>2</sub>. The present work provides a promising, economical, and green strategy for H<sub>2</sub> production along with the synthesis of metal-semiconductor heterostructures, and offers an alternative approach to solar H<sub>2</sub> production and catalyst synthesis. Furthermore, preliminary studies show that this strategy of the direct use of precursor suspensions can be applied to other metal systems and sulphide semiconductors, and will be discussed in more detail in future work.

### Acknowledgements

This research has been supported and funded by European Union's Horizon 2020 research and innovation programme under the Marie Skłodowska-Curie grant agreement No. 892213-USHP to P.S. We acknowledge Prof. Michael Bowker for his advice and support. We thank Diamond Light Source for access and support in the use of the electron Physical Science Imaging Centre (Instrument E01 and E02 and proposal number MG31082) that contributed to the results presented here. The X-ray photoelectron (XPS) data collection was performed at the EPSRC National Facility for XPS ("HarwellXPS"), operated by Cardiff University and UCL, under Contract No. PR16195. We are grateful for support from the UK Catalysis Hub which is funded by EPSRC grant: EP/R026939/1, EP/R026815/1, EP/R026645/1, EP/R027129/1. Access to the XAS beamline was provided through the UK Catalysis Hub Block Allocation Group (BAG), allocation SP29271-5. We thank the Research Complex, Central Laser Facility, Science and Technology Facilities Council (STFC) for access to their facilities and equipment. We thank Dr. Ajay Jha for his help in the Raman spectroscopy measurement.

## Conflict of Interest

The authors declare no conflict of interest.

## Data Availability Statement

The data that support the findings of this study are available in the supplementary material of this article.

**Keywords:** Hydrogen Production · Photocatalysis · Photocatalyst Synthesis Free · Solar Energy Assisted Material Synthesis · in Situ Single Atom Pt Decorated CdS (Pt<sub>SA</sub>-CdS)<sub>IS</sub> Synthesis

- [1] Q. Wang, K. Domen, *Chem. Rev.* **2020**, *120*, 919–985.
- [2] J. L. White, M. F. Baruch, J. E. Pander, Y. Hu, I. C. Fortmeyer, J. E. Park, T. Zhang, K. Liao, J. Gu, Y. Yan, T. W. Shaw, E. Abelev, A. B. Bocarsly, *Chem. Rev.* **2015**, *115*, 12888–12935.
- [3] M. Ko, Y. Kim, J. Woo, B. Lee, R. Mehrotra, P. Sharma, J. Kim, S. W. Hwang, H. Y. Jeong, H. Lim, S. H. Joo, J. W. Jang, J. H. Kwak, *Nat. Catal.* **2022**, *5*, 37–44.
- [4] H. Hou, X. Zeng, X. Zhang, *Angew. Chem. Int. Ed.* **2020**, *59*, 17356–17376; *Angew. Chem.* **2020**, *132*, 17508–17529.
- [5] J. H. Kim, D. Hansora, P. Sharma, J.-W. Jang, J. S. Lee, *Chem. Soc. Rev.* **2019**, *48*, 1908–1971.
- [6] A. Fujishima, K. Honda, *Nature* **1972**, *238*, 37–38.
- [7] T. Takata, J. Jiang, Y. Sakata, M. Nakabayashi, N. Shibata, V. Nandal, K. Seki, T. Hisatomi, K. Domen, *Nature* **2020**, *581*, 411–414.
- [8] H. Nishiyama, T. Yamada, M. Nakabayashi, Y. Maehara, M. Yamaguchi, Y. Kuromiya, Y. Nagatsuma, H. Tokudome, S. Akiyama, T. Watanabe, R. Narushima, S. Okunaka, N. Shibata, T. Takata, T. Hisatomi, K. Domen, *Nature* **2021**, *598*, 304–307.
- [9] P. Sharma, T. J. A. Slater, M. Sharma, M. Bowker, C. R. A. Catlow, *Chem. Mater.* **2022**, *34*, 5511–5521.
- [10] C. M. Wolff, P. D. Frischmann, M. Schulze, B. J. Bohn, R. Wein, P. Livadas, M. T. Carlson, F. Jäckel, J. Feldmann, F. Würthner, J. K. Stolarczyk, *Nat. Energy* **2018**, *3*, 862–869.
- [11] Y. Li, Y.-K. Peng, L. Hu, J. Zheng, D. Prabhakaran, S. Wu, T. J. Puchtler, M. Li, K.-Y. Wong, R. A. Taylor, S. C. E. Tsang, *Nat. Commun.* **2019**, *10*, 4421.
- [12] Q. Wang, M. Nakabayashi, T. Hisatomi, S. Sun, S. Akiyama, Z. Wang, Z. Pan, X. Xiao, T. Watanabe, T. Yamada, N. Shibata, T. Takata, K. Domen, *Nat. Mater.* **2019**, *18*, 827–832.
- [13] Q. Wang, T. Hisatomi, Q. Jia, H. Tokudome, M. Zhong, C. Wang, Z. Pan, T. Takata, M. Nakabayashi, N. Shibata, Y. Li, I. D. Sharp, A. Kudo, T. Yamada, K. Domen, *Nat. Mater.* **2016**, *15*, 611–615.
- [14] J. Liu, Y. Liu, N. Liu, Y. Han, X. Zhang, H. Huang, Y. Lifshitz, S.-T. Lee, J. Zhong, Z. Kang, *Science* **2015**, *347*, 970–974.
- [15] K. Iwashina, A. Iwase, Y. H. Ng, R. Amal, A. Kudo, *J. Am. Chem. Soc.* **2015**, *137*, 604–607.
- [16] X. Meng, S. Wang, C. Zhang, C. Dong, R. Li, B. Li, Q. Wang, Y. Ding, *ACS Catal.* **2022**, *12*, 10115–10126.
- [17] K. Wu, P. Wu, J. Zhu, C. Liu, X. Dong, J. Wu, G. Meng, K. Xu, J. Hou, Z. Liu, X. Guo, *Chem. Eng. J.* **2019**, *360*, 221–230.
- [18] X. Wang, G. Liu, L. Wang, Z.-G. Chen, G. Q. M. Lu, H.-M. Cheng, *Adv. Energy Mater.* **2012**, *2*, 42–46.
- [19] D. Lang, T. Shen, Q. Xiang, *ChemCatChem* **2015**, *7*, 943–951.
- [20] F. M. Zhang, J. L. Sheng, Z. Di Yang, X. J. Sun, H. L. Tang, M. Lu, H. Dong, F. C. Shen, J. Liu, Y. Q. Lan, *Angew. Chem. Int. Ed.* **2018**, *57*, 12106–12110; *Angew. Chem.* **2018**, *130*, 12282–12286.
- [21] R. Lin, L. Shen, Z. Ren, W. Wu, Y. Tan, H. Fu, J. Zhang, L. Wu, *Chem. Commun.* **2014**, *50*, 8533.
- [22] M. Zhang, S. Nie, T. Cheng, Y. Feng, C. Zhang, L. Zheng, L. Wu, W. Hao, Y. Ding, *Nano Energy* **2021**, *90*, 106635.
- [23] M. Zhang, C. Qin, W. Sun, C. Dong, J. Zhong, K. Wu, Y. Ding, *Chin. J. Catal.* **2022**, *43*, 1818–1829.
- [24] Y. Hong, Y. Cho, E. M. Go, P. Sharma, H. Cho, B. Lee, S. M. Lee, S. O. Park, M. Ko, S. K. Kwak, C. Yang, J. W. Jang, *Chem. Eng. J.* **2021**, *418*, 129346.
- [25] P. P. Bag, X.-S. Wang, P. Sahoo, J. Xiong, R. Cao, *Catal. Sci. Technol.* **2017**, *7*, 5113–5119.
- [26] Y. Zhang, J. Zhao, H. Wang, B. Xiao, W. Zhang, X. Zhao, T. Lv, M. Thangamuthu, J. Zhang, Y. Guo, J. Ma, L. Lin, J. Tang, R. Huang, Q. Liu, *Nat. Commun.* **2022**, *13*, 58.
- [27] Y. Chen, S. Ji, W. Sun, Y. Lei, Q. Wang, A. Li, W. Chen, G. Zhou, Z. Zhang, Y. Wang, L. Zheng, Q. Zhang, L. Gu, X. Han, D. Wang, Y. Li, *Angew. Chem. Int. Ed.* **2020**, *59*, 1295–1301; *Angew. Chem.* **2020**, *132*, 1311–1317.
- [28] X. Wu, H. Zhang, J. Dong, M. Qiu, J. Kong, Y. Zhang, Y. Li, G. Xu, J. Zhang, J. Ye, *Nano Energy* **2018**, *45*, 109–117.
- [29] Q. Han, B. Wang, J. Gao, L. Qu, *Angew. Chem. Int. Ed.* **2016**, *55*, 10849–10853; *Angew. Chem.* **2016**, *128*, 11007–11011.
- [30] H. Yang, M. Zhao, J. Zhang, J. Ma, P. Wu, W. Liu, L. Wen, *J. Mater. Chem. A* **2019**, *7*, 20742–20749.
- [31] S. Wang, T. He, P. Chen, A. Du, K. (Ken) Ostrikov, W. Huang, L. Wang, *Adv. Mater.* **2020**, *32*, 2001385.
- [32] O. E. Dagdeviren, D. Glass, R. Sapienza, E. Cortés, S. A. Maier, I. P. Parkin, P. Grütter, R. Quesada-Cabrera, *Nano Lett.* **2021**, *21*, 8348–8354.
- [33] S. Feng, T. Wang, B. Liu, C. Hu, L. Li, Z. Zhao, J. Gong, *Angew. Chem. Int. Ed.* **2020**, *59*, 2044–2048; *Angew. Chem.* **2020**, *132*, 2060–2064.
- [34] T. Li, J. He, B. Peña, C. P. Berlinguette, *Angew. Chem. Int. Ed.* **2016**, *55*, 1769–1772; *Angew. Chem.* **2016**, *128*, 1801–1804.
- [35] Y. P. Xie, Z. B. Yu, G. Liu, X. L. Ma, H.-M. Cheng, *Energy Environ. Sci.* **2014**, *7*, 1895.
- [36] J. Resasco, L. Derita, S. Dai, J. P. Chada, M. Xu, X. Yan, J. Finzel, S. Hanukovich, A. S. Hoffman, G. W. Graham, S. R. Bare, X. Pan, P. Christopher, *J. Am. Chem. Soc.* **2020**, *142*, 169–184.
- [37] X. Li, W. Bi, L. Zhang, S. Tao, W. Chu, Q. Zhang, Y. Luo, C. Wu, Y. Xie, *Adv. Mater.* **2016**, *28*, 2427–2431.
- [38] Z. Teng, Q. Zhang, H. Yang, K. Kato, W. Yang, Y. R. Lu, S. Liu, C. Wang, A. Yamakata, C. Su, B. Liu, T. Ohno, *Nat. Catal.* **2021**, *4*, 374–384.
- [39] Y. Zhao, H. Zhou, X. Zhu, Y. Qu, C. Xiong, Z. Xue, Q. Zhang, X. Liu, F. Zhou, X. Mou, W. Wang, M. Chen, Y. Xiong, X. Lin, Y. Lin, W. Chen, H. J. Wang, Z. Jiang, L. Zheng, T. Yao, J. Dong, S. Wei, W. Huang, L. Gu, J. Luo, Y. Li, Y. Wu, *Nat. Catal.* **2021**, *4*, 134–143.
- [40] J. A. Nasir, Z. U. Rehman, S. N. A. Shah, A. Khan, I. S. Butler, C. R. A. Catlow, *J. Mater. Chem. A* **2020**, *8*, 20752–20780.
- [41] C. Chen, Y. Kang, Z. Huo, Z. Zhu, W. Huang, H. L. Xin, J. D. Snyder, D. Li, J. A. Herron, M. Mavrikakis, M. Chi, K. L. More, Y. Li, N. M. Markovic, G. A. Somorjai, P. Yang, V. R. Stamenkovic, *Science* **2014**, *343*, 1339–1343.
- [42] K. L. Zhou, Z. Wang, C. B. Han, X. Ke, C. Wang, Y. Jin, Q. Zhang, J. Liu, H. Wang, H. Yan, *Nat. Commun.* **2021**, *12*, 3783.
- [43] Z. Liu, S. Ma, L. Chen, J. Xu, J. Ou, M. Ye, *Mater. Chem. Front.* **2019**, *3*, 851–859.
- [44] P. Xie, T. Pu, A. Nie, S. Hwang, S. C. Purdy, W. Yu, D. Su, J. T. Miller, C. Wang, *ACS Catal.* **2018**, *8*, 4044–4048.
- [45] Y. Shi, Z.-R. Ma, Y.-Y. Xiao, Y.-C. Yin, W.-M. Huang, Z.-C. Huang, Y.-Z. Zheng, F.-Y. Mu, R. Huang, G.-Y. Shi, Y.-Y. Sun, X.-H. Xia, W. Chen, *Nat. Commun.* **2021**, *12*, 3021.

- [46] A. Z. Jovanović, L. Bijelić, A. S. Dobrota, N. V. Skorodumova, S. V. Mentus, I. A. Pašti, *Electrochim. Acta* **2022**, *414*, 140214.
- [47] S. Bai, B. Huang, Q. Shao, X. Huang, *ACS Appl. Mater. Interfaces* **2018**, *10*, 22257–22263.
- [48] K. Ding, A. Gulec, A. M. Johnson, N. M. Schweitzer, G. D. Stucky, L. D. Marks, P. C. Stair, *Science* **2015**, *350*, 189–192.
- [49] X. Shi, C. Dai, X. Wang, J. Hu, J. Zhang, L. Zheng, L. Mao, H. Zheng, M. Zhu, *Nat. Commun.* **2022**, *13*, 1287.
- [50] B. Qiao, A. Wang, X. Yang, L. F. Allard, Z. Jiang, Y. Cui, J. Liu, J. Li, T. Zhang, *Nat. Chem.* **2011**, *3*, 634–641.
- [51] L. Wang, M.-X. Chen, Q.-Q. Yan, S.-L. Xu, S.-Q. Chu, P. Chen, Y. Lin, H.-W. Liang, *Sci. Adv.* **2019**, *5*, eaax6322.
- [52] J. Zhu, L. Cai, X. Yin, Z. Wang, L. Zhang, H. Ma, Y. Ke, Y. Du, S. Xi, A. T. S. Wee, Y. Chai, W. Zhang, *ACS Nano* **2020**, *14*, 5600–5608.
- [53] Y. Zhu, T. Cao, C. Cao, J. Luo, W. Chen, L. Zheng, J. Dong, J. Zhang, Y. Han, Z. Li, C. Chen, Q. Peng, D. Wang, Y. Li, *ACS Catal.* **2018**, *8*, 10004–10011.
- [54] Q.-Q. Yan, D.-X. Wu, S.-Q. Chu, Z.-Q. Chen, Y. Lin, M.-X. Chen, J. Zhang, X.-J. Wu, H.-W. Liang, *Nat. Commun.* **2019**, *10*, 4977.
- [55] C. Han, Z.-R. Tang, J. Liu, S. Jin, Y.-J. Xu, *Chem. Sci.* **2019**, *10*, 3514–3522.
- [56] V. Dzhagan, A. G. Milekhin, M. Y. Valakh, S. Pedetti, M. Tessier, B. Dubertret, D. R. T. Zahn, *Nanoscale* **2016**, *8*, 17204–17212.

Manuscript received: January 24, 2023

Accepted manuscript online: February 14, 2023

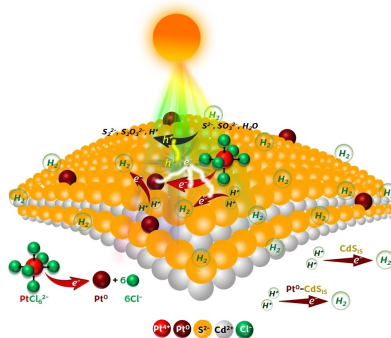
Version of record online: ■■■■■

## Research Articles

Photocatalytic H<sub>2</sub> Evolution

P. Sharma,\* M. Sharma, M. Dearg,  
M. Wilding, T. J. A. Slater,  
C. R. A. Catlow\* \_\_\_\_\_ e202301239

Cd/Pt Precursor Solution for Solar H<sub>2</sub>  
Production and in situ Photochemical Syn-  
thesis of Pt Single-atom Decorated CdS  
Nanoparticles



This work reports the use of Cd/Pt precursor solutions for substantially higher photocatalytic H<sub>2</sub> production (154.7 mmol g<sup>-1</sup> h<sup>-1</sup>), thereby eliminating the need for pre-synthesized photocatalysts for H<sub>2</sub> production. Furthermore, in parallel to H<sub>2</sub> production, a simplified solar light-assisted in situ synthesis of Pt single-atom anchored CdS nanoparticles (Pt<sub>SA</sub>-CdS<sub>IS</sub>) has also been demonstrated.